Ru–modified graphitic carbon nitride for the solar light–driven photocatalytic H2O2 synthesis

Laura Valenzuela, Frael-Benjamin Yimbou, Antoine Ewin, Christophe Lefèvre, Ramón Manzorro, Nicolas Keller

Ru–modified graphitic carbon nitride for the solar light–driven photocatalytic H_2O_2 synthesis

Laura Valenzuela,[a,*] Frael-Benjamin Yimbou,[a] Antoine Ewin,[a] Christophe Lefèvre,[b] Ramón Manzorro,[c] Nicolas Keller [a]

[a] Institut de Chimie et Procédés pour l'Energie, l'Environnement et la Santé (ICPEES), CNRS, Strasbourg University, 25 rue Becquerel, 67087, Strasbourg, France.

[b] Institut de Physique et de Chimie des Matériaux de Strasbourg (IPCMS), CNRS/Strasbourg University, 23 rue du Loess, Strasbourg, France.

[c] Departamento de Ciencias de los Materiales e Ingeniería Metalúrgica y Química Inorgánica, Facultad de Ciencias, Universidad de Cádiz, Spain.

[*] *Corresponding author:* valenzuelaavila@unistra.fr (L. Valenzuela)

Abstract

Hydrogen peroxide (H_2O_2) is an efficient and environmentally friendly oxidant as well as a promising energy-carrier alternative to hydrogen. Its solar light-driven photocatalytic synthesis from H_2O and O_2 is a high-prospect sustainable alternative to the industrial anthraquinone process. Hybrid Ru-modified graphitic carbon nitride (g-C_3N_4) catalysts were prepared by thermal polymerisation of melamine/Ru(III) acetylacetonate mixtures, and subsequent thermal exfoliation. Simultaneous Ru incorporation and thermal exfoliation impacted the morphology and the structure of the g-C_3N_4 sheets, and low-atomicity Ru species with small nanoclusters and single atoms were observed only in the Ru-modified exfoliated g-C_3N_4 photocatalysts. We demonstrated the potential of a joint

thermal exfoliation and modification with Ru to enhance the H_2O_2 synthesis efficiency of the g-C_3N_4 photocatalyst under simulated sunlight. A volcano-type behavior was observed with increasing the Ru content, and the best performance was obtained for exfoliated g-C_3N_4 with an ultra-low Ru content of 0.019 *wt*.%, that outperformed both its bulk counterpart and the pristine exfoliated reference in terms of initial H_2O_2 synthesis rate and H_2O_2 formation rate constant. The enhanced performance was attributed to the presence of highly dispersed low atomicity Ru as well as to more accessible active sites and carrier migration channels. Quenching experiments revealed a mixed reactional pathway involving both two-step one-electron and one-step two-electron O_2 reduction in the photocatalytic H_2O_2 production.

Keywords: Hydrogen peroxide; Photocatalysis; Graphitic carbon nitride; Ruthenium; Thermal exfoliation

1. Introduction

Hydrogen peroxide (H_2O_2) is an efficient and environmentally friendly oxidant due to its large active oxygen content (47 *wt*.%), relatively high oxidation potential (E°=1.763V *vs*. NHE at pH 0), easy-handling and non-toxic oxidation by-products (water and oxygen) [1, 2]. These properties make H_2O_2 suitable for varied applications like wastewater treatment (*eg*., Fenton processes and disinfection), chemical manufacturing or pulp bleaching, with an annual worldwide production over 5 Mt [2, 3]. Moreover, H_2O_2 is a promising energy-carrier alternative to hydrogen, since it can be used as fuel in single-compartment cells and can be conveniently transported and stored [4]. Currently, H_2O_2 is produced industrially by the well-known high E-factor and low atom efficiency multi-

52 step anthraquinone process, which requires high energy input and generates large
53 amounts of wastes (*eg.* organics-containing wastewater, solid waste) [1, 2].

54 Therefore, it is worthwhile to develop cost-effective and sustainable approaches for
55 H_2O_2 production. In this context, solar light-driven photocatalysis has emerged as it
56 utilizes H_2O and molecular O_2 as raw materials, and solar light as energy supply [5, 6].
57 Photocatalysis is also a worth strategy for the safe and cost-efficient implementation of
58 decentralized small-scale production units as well as for the *in-situ* synthesis of H_2O_2 for
59 use as oxidant in high-efficiency chemical reactions [7].

60 Graphitic carbon nitride (g-C_3N_4) is a prominent candidate for H_2O_2 production
61 because of its relatively narrow band gap (*ca*. 2.7 eV), suitable electronic structure for O_2
62 reduction and a high chemical stability [8]. g-C_3N_4 benefits also from easy, low-cost
63 preparation methods, as well as from its metal-free and non-toxic nature. Shiraishi et al.
64 [9] first reported the ability of g-C_3N_4 to selectively produce H_2O_2 (>90%) under visible
65 light in water/alcohol mixtures owing to the formation of 1,4-endoperoxide species as
66 surface intermediates. However, bulk g-C_3N_4 obtained by thermal polymerisation still
67 suffers from fast recombination of photogenerated electron/hole pairs, weak electrical
68 conductivity, low surface area and poor dispersion in water [8, 10].

69 Several methods have been explored to improve the photocatalytic activity of g-
70 C_3N_4, including nanoarchitecture and defect engineering [11], metal or non-metal doping
71 [6, 12], decoration with metal nanoparticles [13], molecular engineering [14] or
72 heterojunction construction [15]. Thermal exfoliation of bulk g-C_3N_4 into two-
73 dimensional nanosheets has been highlighted as a simple and effective strategy to increase
74 its specific surface area, provide more accessible active sites, enhance its dispersibility,
75 and facilitate charge carrier separation [16, 17]. In this regard, transition metal doping of
76 the g-C_3N_4 framework with simultaneous morphology engineering can promote the

77 synthesis of H_2O_2 [5, 6, 18]. As the synthesis of H_2O_2 can occur by partial oxidation of
78 water or O_2 reduction involving a hydrogenation step, and Ru being is a well-known
79 hydrogenation catalyst [19] that has demonstrated to promote water oxidation [20], it
80 worth investigating to which extent the photocatalytic synthesis of H_2O_2 can be enhanced
81 by modifying g-C_3N_4 with Ru. Among transition metals, the unique electronic
82 configuration of Ru as $4d^7 5s^1$, allowing variable oxidation states and complex coordinate
83 geometries, has made it an outstanding catalyst in many reactions. Previous works
84 showed that anchoring RuP complexes at the surface of g-C_3N_4 and stabilizing Ru
85 nanoparticles on metal-organic-frameworks enhanced the photocatalytic production of
86 solar H_2 or the photodegradation of organic pollutants, respectively, owing to a lower
87 charge carrier recombination that results from their ability to capture electrons and from
88 the formation of intermediate energy levels [21, 22].
89 Thus, we aim hereby at reporting for the first time to which extent the activity of a
90 g-C_3N_4 reference photocatalyst can be enhanced under simulated solar irradiation by
91 incorporating Ru. Hybrid photocatalysts were prepared by thermal polymerisation of
92 melamine/ruthenium(III) acetylacetonate mixtures. We demonstrated the potential of
93 simultaneous thermal exfoliation and modification with ultra-low amounts of Ru to
94 improve the photocatalytic H_2O_2 generation efficiency of the g-C_3N_4 materials under
95 simulated solar irradiation.
96

97 ## 2. Materials and methods

98

99 ### 2.1. Chemicals

100 The chemicals used are described in SI1.
101

2.2. Synthesis of Ru-modified g-C_3N_4 catalysts

Bulk g-C_3N_4 (BCN) was synthesized by thermal polymerisation of melamine under static air atmosphere in a muffle furnace. Briefly, 14 g of melamine was placed in a lidded alumina crucible (60 mL) and heated at 550℃ for 4 h (5℃/min). After naturally cooling down to room temperature, the pale-yellow product obtained was ground into powder, and further subjected to a typical thermal exfoliation procedure at 550℃ for 4 h (5℃/min) to yield g-C_3N_4 nanosheets (TCN). Ru-modified g-C_3N_4 catalysts were synthesized by a similar two-step process, in which $Ru(acac)_3$ was first added to melamine with different mass ratios by finely grinding in a mortar. The photocatalysts were denoted as *x*Ru-BCN and *x*Ru-TCN for Ru-modified bulk and exfoliated g-C_3N_4, respectively, where *x* refers to the final Ru content (*wt*.%) as determined by elemental chemical analysis.

2.3. Characterisation of Ru-modified g-C_3N_4 catalysts

The crystalline structure of the g-C_3N_4 materials was assessed by X-ray diffraction (XRD, Bruker D8-Advance diffractometer) using Cu Kα radiation (λ=1.54Å). Zero-shift was determined by performing additional XRD analysis using mixtures of the photocatalysts with 5 *wt*.% of highly-crystallized NaCl (space group Fm-3m with cell parameter 5.64056Å). Fitting of the patterns was performed over the 21-36° 2θ range of interest using a pseudo-Voigt function for both the (002) plane of g-C3N4 and the (200) plane of NaCl (COD 00-900-8678).

Their morphology was investigated by advanced scanning/transmission electron microscopy (STEM) using a double aberration-corrected monochromated FEI Titan Cubed Themis 60-300 working at 300 kV. High angle annular dark field (HAADF) images were acquired. Analytical information at the atomic scale was provided by energy-

dispersive X-ray spectroscopy (EDX), collecting the signal in the four-detectors Super X-G2 capabilities, which allow to track the elemental distribution.

The Ru content in g-C_3N_4 was determined by inductively coupled plasma-atomic emission spectroscopy (ICP-AES, Perkin Elmer Optima 7000DV) after acidic digestion in microwave oven at 185°C.

Additionally, the photocatalysts were characterized by UV-vis diffuse reflectance spectroscopy (DRS) and N_2 adsorption-desorption isotherms. Experimental details are provided in SI2.

2.4. Photocatalytic synthesis of H_2O_2

Photocatalytic H_2O_2 production experiments were conducted in a beaker-type glass reactor at a constant temperature of 20±5°C (using a cooling bath) under simulated solar irradiation, provided by a Suntest XLS+ reaction chamber (Atlas Material Testing Technology BV) equipped with a 1700W Xenon arc lamp providing an irradiance of 500 $W.m^{-2}$. 100 mg photocatalyst was dispersed in 100 mL aqueous solution containing 5% *v/v* isopropyl alcohol (IPA) as hole (h^+) scavenger. Prior to irradiation, the catalyst suspension was stirred at 500 rpm for 15 min in the dark to ensure the establishment of the adsorption-desorption equilibrium. The dispersion was bubbled with synthetic air at 10 $mL.min^{-1}$ for saturating the system with O_2. Samples of 4 mL were withdrawn at given time intervals and immediately filtered (PES, 0.22 μm) to separate the catalyst and measure the H_2O_2 concentration by iodometry, as described in SI3 [23].

Additional tests were performed under pure visible light irradiation using a 420 nm cut-off filter (GG420 Yellow Schott Optical Filters). The emission spectra of the light sources were measured with a portable wideband RPS900-W spectroradiometer (International Light Technology) (Fig. S1).

Quenching experiments were conducted to determine the main active species in the reaction. To that end, 1 mM of *p*-BQ and $AgNO_3$ were added separately to ultrapure water to scavenge superoxide ($O_2^{\bullet-}$) and photogenerated electrons (e^-), respectively.

3. Results and discussion

3.1. Characterisation of the photocatalysts

Table 1 shows the main physico-chemical properties derived from the XRD and the ICP-AES analyses. The g-C_3N_4 based photocatalysts displayed very low weight contents of Ru, namely within the 0.006-0.049 *wt.*% and 0.011-0.054 *wt.*% ranges for both *x*Ru-BCN and *x*Ru-TCN series, respectively.

The XRD patterns shown in Fig. 1a-b and Fig. S2 exhibited the characteristic peaks of graphitic carbon nitride for all samples (JCPDS 87–1526). The intense diffraction peak at 27.6° was assigned to the (002) plane, attributed to the interlayer stacking of the conjugated aromatic system with an inter-planar distance of 3.2 Å. The ill-defined low-intensity peak at 12.8° corresponded to the (100) plane, related to the in-plane structural packing motif of the tris-*s*-triazine units with a period of 6.9 Å (Table 1) [17, 24, 25]. Incorporating Ru did not modify the basic structure of g-C_3N_4, and no Ru-related diffraction peaks were observed probably because of its low loading (≤0.054 *wt.*%).

After zero-shift correction, Fig. 1c-d and Table 1 show that both the exfoliation process and the presence of very low-content Ru influenced the crystallographic features of the g-C_3N_4. In the absence of Ru, exfoliation led to a slight shift of the (002) peak towards larger angles, indicating a reduced inter-planar distance and suggesting stronger interlayer interaction with a higher number of staked layers [26, 27]. The full width at half-maximum (FWHM) of the (002) peak decreased after thermal treatment, resulting in

176 a higher number of stacked layers and an increased crystal thickness. A reduced FWHM
177 also relates to a higher degree of crystallinity, what promotes the tighter packing of layers
178 [27, 28]. Thus, it suggests higher crystallinity for TCN and exfoliated *x*Ru-TCN
179 compared to the bulk *x*Ru-BCN series. Interestingly, very low-content Ru increased the
180 inter-planar distance and decreased both crystal thickness and number of stacked layers
181 compared to pristine materials, the effect being by far more pronounced for the exfoliated
182 *x*Ru-TCN series with a clear volcano-curve centred around x = 0.011-0.019 *wt*.%.

183 Compared to the bulk *x*Ru-BCN series, the (100) peak intensity of exfoliated g-
184 C_3N_4 (TCN and *x*Ru-TCN) decreased to some extent, and more significantly as the Ru
185 content increased, indicating a reduction in the lateral size of the graphitic layers when
186 performing the exfoliation in the presence of Ru [16, 17, 24]. This might be related to the
187 lower yields to g-C_3N_4 obtained for the *x*Ru-TCN samples when the Ru content increased,
188 that reflect the decomposition of g-C_3N_4 to gaseous products during the thermal treatment
189 (Table 1). Non-exhaustive explanations of the lower yields obtained rely on the presence
190 of Ru within the *x*Ru-BCN samples that might favor the over-oxidation of the g-C_3N_4, as
191 it slightly lowers the crystallinity of bulk materials, might induce local increase in
192 temperature during exfoliation, or provide a higher amount of surface sites exposed for
193 reacting with molecular oxygen. However, the ill-defined nature and low-intensity of the
194 (100) diffraction peak prevented the assessment of whether the presence of Ru during the
195 exfoliation modified the in-plane periodicity of the tris-*s*-triazine units.
196

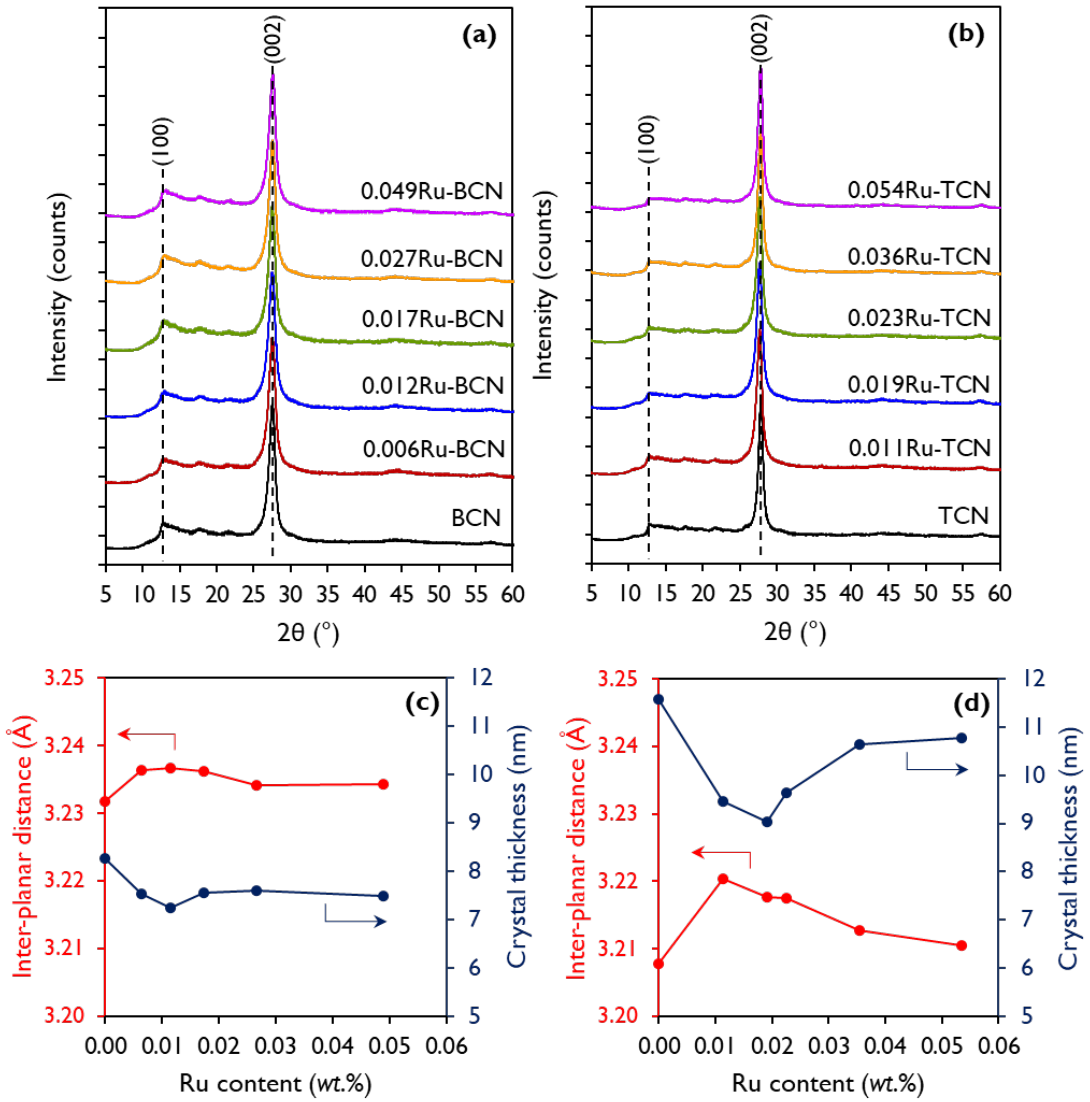

197

198

199 **Figure 1.** X-ray diffraction patterns of Ru-modified bulk g-C_3N_4 photocatalysts, **(a)** *x*Ru-
200 BCN and **(b)** Ru-modified exfoliated g-C_3N_4, *x*Ru-TCN. Influence of the Ru content on
201 the inter-planar distance and crystal thickness for **(c)** *x*Ru-BCN and **(d)** *x*Ru-TCN
202 photocatalysts.

Table 1. Ru content, yield to g-C_3N_4, structural parameters obtained from XRD results (tris-*s*-triazine unit distance, inter-planar distance, crystal thickness, number of stacked layers), band gap energies, BET surface area and pore volume.

Catalysts	Ru content (*wt.* %) [a]	Yield to g-C_3N_4 (%) [b]	I(100)/ I(002) [c]	Tris-*s*-triazine unit distance (Å) [d]	Inter-planar distance (Å) [e]	Crystal thickness (nm) [f]	Number of stacked layers [g]	Band gap energies (eV) [h]	BET surface area [*t*-plot micropore area] ($m^2 g^{-1}$)	Pore volume ($m^3 g^{-1}$)
BCN	-	42	0.19	6.916	3.232	8.3	26	2.69	21 [16]	0.24
0.006Ru-BCN	0.006	43	0.18	6.917	3.236	7.5	23	2.73	24 [6]	0.17
0.012Ru-BCN	0.012	43	0.18	6.916	3.237	7.2	22	2.73	25 [9]	0.12
0.017Ru-BCN	0.017	42	0.22	6.915	3.236	7.6	23	2.73	28 [10]	0.14
0.027Ru-BCN	0.027	42	0.21	6.915	3.234	7.6	23	2.73	32 [5]	0.16
0.049Ru-BCN	0.049	41	0.21	6.916	3.234	7.5	23	2.73	26 [12]	0.14
TCN	-	23	0.13	6.917	3.208	11.6	36	2.73	51 [26]	0.42
0.011Ru-TCN	0.011	24	0.12	6.917	3.220	9.5	29	2.75	71 [14]	0.37
0.019Ru-TCN	0.019	21	0.12	6.915	3.218	9.0	28	2.76	76 [13]	0.41
0.023Ru-TCN	0.023	20	0.11	6.916	3.218	9.6	30	2.77	88 [17]	0.38
0.036Ru-TCN	0.036	16	0.10	6.915	3.213	10.6	33	2.77	100 [17]	0.43
0.054Ru-TCN	0.054	12	0.09	6.917	3.211	10.8	34	2.79	107 [21]	0.34

[a] Ru content measured by ICP-AES analysis.
[b] Yield to g-C_3N_4 determined as the mass ratio of the g-C_3N_4 material (bulk or exfoliated) to the melamine reactant.
[c] I(100)/I(002) determined as the intensity ratio of the (100) to the (002) planes.
[d] Tris-*s*-triazine unit distance calculated through Bragg equation using the (100) plane.
[e] Inter-planar distance determined through Bragg equation using the (002) plane.
[f] Crystal thickness calculated by the Debye-Scherrer equation using the (002) plane.
[g] Number of stacked layers determined as the ratio of the crystal thickness to the inter-planar distance.
[h] Band gap energies estimated through Kubelka-Munk function combined with Tauc's relation and baseline method.

The optical properties of the g-C_3N_4-based photocatalysts were studied by UV-vis DRS (Fig. S3). All photocatalysts exhibited the characteristic absorption edge of g-C_3N_4 [25], with indirect band gaps being estimated at *ca.* 2.7 (Table 1) in agreement with reported values [6, 29] and not significantly influenced by the exfoliation process and the addition of Ru (Table 1). Thermally exfoliated materials displayed reduced absorption intensity in both the UV range and the visible region, what has been ascribed to a quantum confinement within the stacked layers [30, 31]. By contrast, the incorporation of Ru to bulk and exfoliated g-C_3N_4 increased the absorption features. This aligns with previous reports on metallic nanoparticles or metal complexes (*e.g.*, Ni or triphenylphosphine ruthenium, RuP) on g-C_3N_4, that indicated the strengthening of light absorption without shifting the absorption edge [5, 21]. No significant difference was observed as regards the valence band edge derived from XPS measurements between the BCN reference and the 0.019Ru-TCN photocatalyst (data not shown).

The specific surface area and porous structure of g-C_3N_4 were analysed through N_2 sorption isotherms (Fig. S4 and Table 1). The isotherms can be classified as type IV with H3 hysteresis loops in the high-pressure region, suggesting the presence of mesopores [30]. Compared to BCN (21 m^2/g), the BET surface area of *x*Ru-BCN followed a volcano-type trend with increasing Ru content, reaching a maximum of 32 m^2/g for 0.027Ru-BCN. The BET surface area of TCN at 51 m^2/g strongly overcame that of BCN, and further gradually increased with increasing Ru content up to the high value of 107 m^2/g for 0.054Ru-TCN. This confirmed that both thermal exfoliation and Ru influenced the morphology of g-C_3N_4 materials. While *t*-plot method reflected the presence of microporosity in all samples, the pore size distribution curves derived from BJH method (Fig. S4 c-d) showed slight modifications due to Ru presence and exfoliation. Both pristine g-C_3N_4 catalysts showed a broad monomodal distribution centred at around 50

and 80 nm for BCN and TCN, respectively. The incorporation of Ru slightly narrowed the pore size distribution for both bulk and exfoliated photocatalyst series. Interestingly, in the presence of Ru, the *x*Ru-TCN photocatalysts developed a slightly bimodal distribution during exfoliation, with the appearance of an additional low-intensity contribution at *ca.* 3 nm of pore size, that is particularly visible for the highest Ru contents. The exfoliated *x*Ru-TCN owned by far larger pore volumes compared to *x*Ru-BCN counterparts (Table 1), probably due to their layered structure. Furthermore, the pore volume of BCN decreased to some extent after Ru modification, while this trend was not observed for the exfoliated materials, for which it remained almost constant except for the 0.054Ru-TCN photocatalyst.

The morphology and elemental distribution of the 0.012Ru-BCN and 0.019Ru-TCN photocatalysts, as representative of both Ru-based g-C_3N_4 series, were investigated by HAADF-STEM and STEM-EDX elemental mapping and compared to the Ru-free TCN reference (Fig. 2 and Fig. S5). A visual inspection of TCN, based on low magnification HAADF images, revealed a more graphitic structure compared to BCN, consistent with the higher crystallinity observed by XRD. Notably, 0.019Ru-TCN exhibited a more porous structure with folds than its bulk g-C_3N_4 counterpart (0.012Ru-BCN), but similar to that of pristine TCN, in agreement with the pore volume analysis. Regarding metal dispersion, low-magnification HAADF-STEM images in combination with STEM-EDX maps of both Ru-modified g-C_3N_4 catalysts (Fig. 2a-b and Fig. 2d-e) indicated the presence of Ru aggregates (> 10 nm), accumulating in some regions of the carbon nitride matrix.

When decreasing in Ru size, exfoliated 0.019Ru-TCN sample presented a higher fraction of Ru nanoparticles with dimensions of *ca.* 5 nm, as illustrated in Fig. S5. However, more interestingly, the most important difference between the two Ru-modified

265 samples laid in the existence of bright spots uniformly distributed at the surface of TCN
266 (Fig. 2f) as opposed to the bare surface in 0.012Ru-BCN material (Fig. 2c). The heavier
267 nature of metallic Ru may suggest the correspondence of bright intensities with highly
268 dispersed Ru species in the form of clusters and even single atoms (< 0.2 nm). Despite its
269 ultra-low content (0.019 *wt.*%), the presence of low-atomicity Ru species in 0.019Ru-
270 TCN (and not in 0.012Ru-BCN) was confirmed by EDX analysis. Given the low
271 dimension of these Ru-based entities, its spatial distribution in an elemental map is not
272 reliable and may be corrupted by noise. However, the integrated spectra over a region of
273 5x5 nm, Fig. 2g, captured the presence of Ru-L peak in the case of 0.019Ru-TCN (black)
274 *vs.* the lack of Ru EDX signal on the 0.012Ru-BCN sample (blue), demonstrating
275 analytically the existence of low-atomicity Ru in the exfoliated sample. In order to better
276 understand the distribution of the Ru species, the HAADF images of the 0.019Ru-TCN
277 photocatalyst have been processed with a tailored protocol based on segmentation
278 methods [32], focusing on the identification of single atoms and low-atomicity species
279 (Fig. 3). The cluster size distribution, with a mean cluster size of 0.20 nm, showed a
280 marked positive skew, this indicating the high population of Ru single atoms.

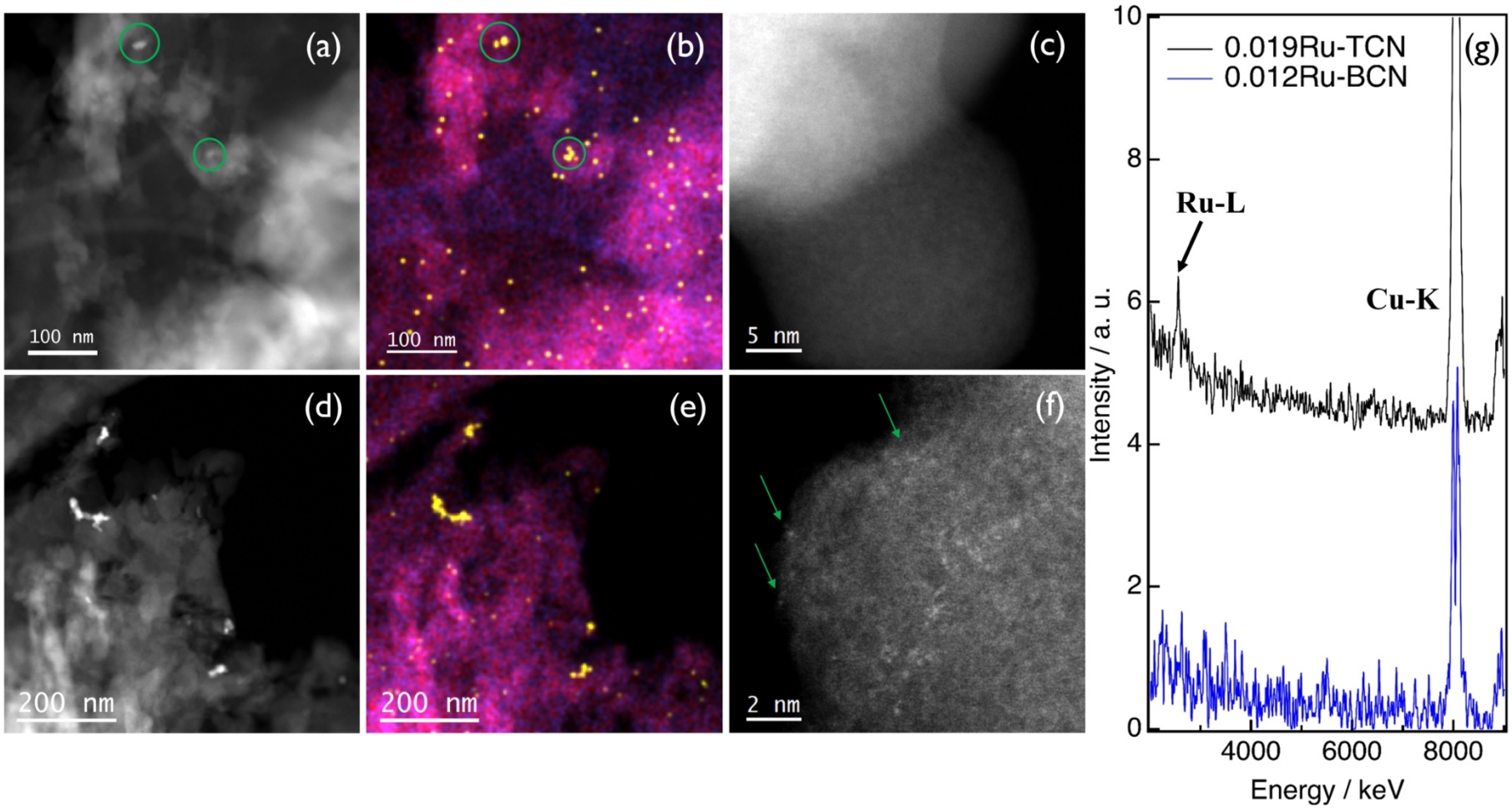

281

282 **Figure 2**. Low and high-magnification HAADF-STEM images, STEM–EDX elemental mappings (C ■, N ■, Ru ■) on both **(a-c)** 0.012Ru-BCN

283 and **(d-f)** 0.019Ru-TCN photocatalysts. **(g)** The corresponding EDX spectra.

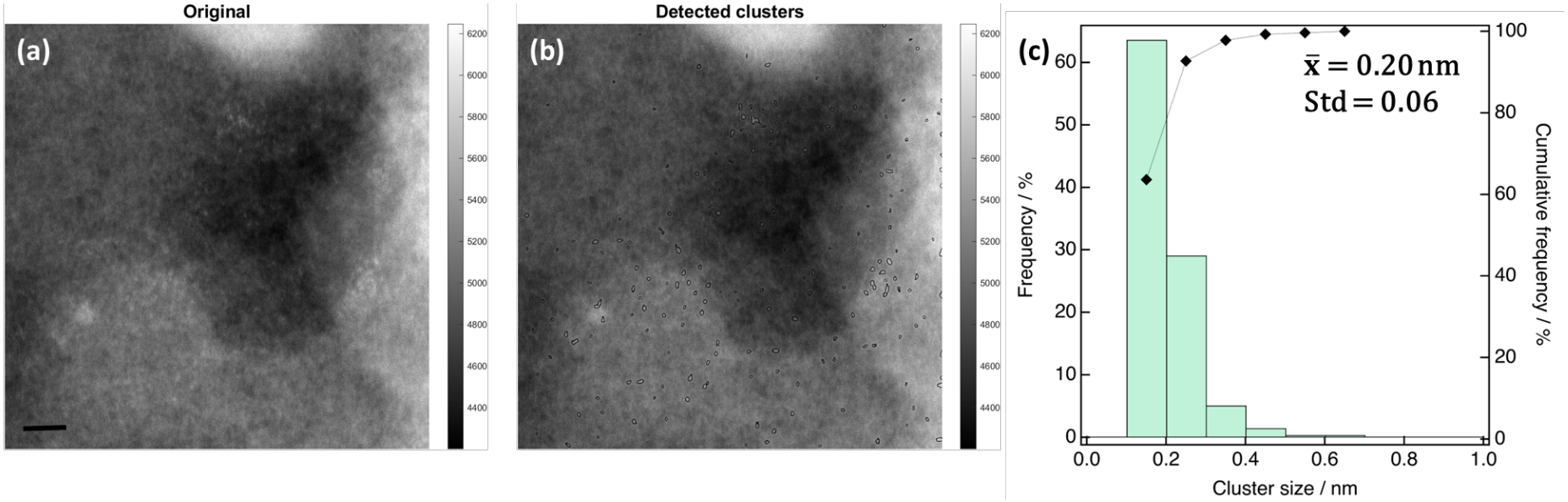

284

285 **Figure 3.** **(a)** Representative HAADF image of the 0.019Ru-TCN sample, **(b)** HAADF image after segmentation procedure to detect Ru

286 clusters, **(c)** cluster size histogram derived from more than 250 Ru species. The scale bar corresponds to 2 nm.

3.2. Photocatalytic synthesis of H_2O_2

3.2.1. Synthesis under solar light

The photocatalytic performance for H_2O_2 production of the Ru-modified g-C_3N_4 materials was evaluated with 5% *v/v* IPA under simulated solar light irradiation and continuous air supply at controlled temperature (20±5℃). As shown in Fig. 4, the pristine BCN and TCN catalysts displayed low photocatalytic activity, with an apparent initial H_2O_2 production rate of 132 ± 5 and 137 ± 14 μmol/g/h, respectively, commonly assessed by a zero-order rate law. Modification of bulk g-C_3N_4 with Ru at ultra-low concentrations (*x*Ru-BCN with $x \leq 0.012$ *wt*.%) slightly improved the catalytic performance, with an increase in the initial H_2O_2 synthesis up to 155 ± 18 and 156 ± 12 μmol/g/h for 0.006Ru-BCN and 0.012Ru-BCN, respectively. Further increase in Ru concentration lowered the initial H_2O_2 production rate. By contrast, the initial H_2O_2 production rate obtained with the exfoliated *x*Ru-TCN followed a strongly pronounced volcano curve as Ru content increased, with a maximum initial rate of 296 ± 8 μmol/g/h for the 0.019Ru-TCN photocatalyst, namely 2.2 times higher than those achieved with pristine BCN and TCN.

However, the overall H_2O_2 production must consider that the H_2O_2 formed can decompose either by absorbing UV light (λ≤400 nm) (1) [33], or by reacting with photogenerated electrons and holes at the catalyst surface [34] (2-5):

$$H_2O_2 \xrightarrow{h\upsilon} 2HO^{\bullet} \quad (1)$$

$$H_2O_2 + H^+ + e^- \rightarrow H_2O + HO^{\bullet} \quad (2)$$

$$H_2O_2 + 2H^+ + 2e^- \rightarrow 2H_2O \quad (3)$$

$$H_2O_2 + h^+ \rightarrow H^+ + HO_2^{\bullet} \quad (4)$$

$$H_2O_2 + 2h^+ \rightarrow O_2 + 2H^+ \quad (5)$$

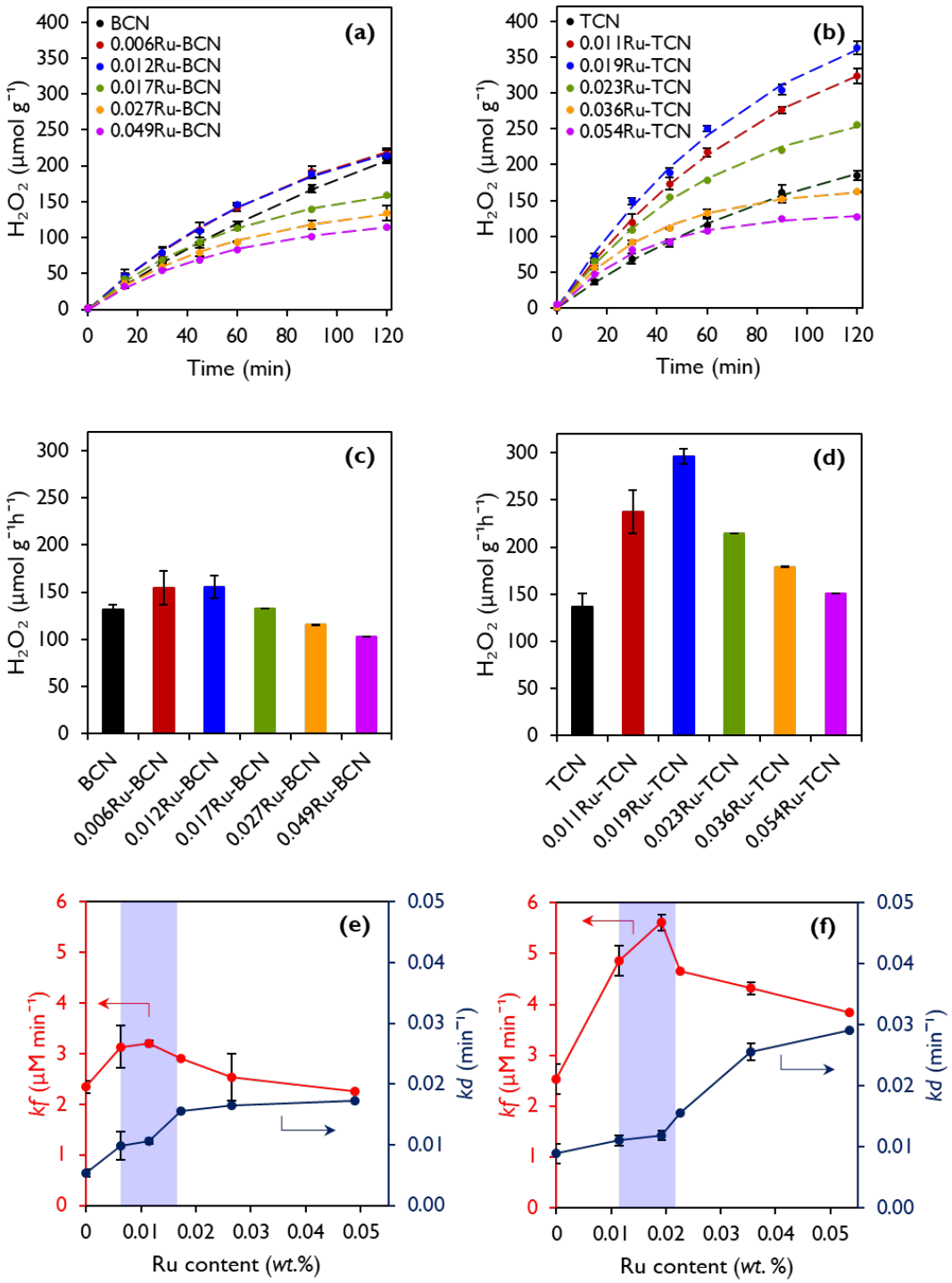

312

313 **Figure 4**. Photocatalytic synthesis of H_2O_2 with kinetic fitting **(a, b)**, initial apparent H_2O_2

314 production rates **(c, d)**, and formation (*kf*) and decomposition (*kd*) rate constants as a

315 function of the Ru content **(e, f)** over Ru-modified bulk g-C_3N_4, *x*Ru-BCN **(a, c, e)**, and

316 Ru-modified exfoliated g-C_3N_4, *x*Ru-TCN **(b, d, f)**, catalysts. Experiments performed

317 with 5% *v/v* IPA under simulated solar light irradiation (500 $W.m^{-2}$).

The H_2O_2 production rate gradually diminishes over time because both generation and decomposition occur simultaneously. Consequently, assessing the apparent kinetic constants for both formation (*kf*, $\mu M.min^{-1}$) and decomposition (*kd,* min^{-1}) is necessary to understand this dynamic process. The accumulated H_2O_2 is commonly evaluated by a zero-order rate law for H_2O_2 formation and a first-order rate law for H_2O_2 decomposition (6) [35]:

$$[H_2O_2] = kf/kd \times \{1 - \exp(-kd \times t)\} \quad (6)$$

where $[H_2O_2]$ denotes the concentration of H_2O_2 (μmol/L) and *t* is the reaction time (min). The *kf* and *kd* values are obtained by fitting the experimental data into Eqn. 6. The kinetic fits are shown in Fig. 4a,b (dashed lines), while the apparent rate constants *kf* and *kd* are plotted in Fig. 4e,f as a function of Ru content in the g-C_3N_4 catalysts.

Considering both kinetics, the results in Fig. 4e,f evidenced that thermal exfoliation promoted both H_2O_2 formation and decomposition rate constants, and in a more pronounced way for *kd* that increased from $0.54 \pm 0.01 \times 10^{-2}$ to $0.88 \pm 0.02 \times 10^{-2}$ min^{-1}, while *kf* only slightly increased from 2.34 ± 0.12 to 2.53 ± 0.30 $\mu M.min^{-1}$. As a result, although the initial H_2O_2 production rate was slightly higher for TCN than for BCN, the concentration of H_2O_2 accumulated after 2 h of reaction with TCN remained lower than that with BCN, *ie*. 185 ± 6 μmol/g/h *vs.* 208 ± 3 μmol/g/h. Concerning the Ru-modified g-C_3N_4 photocatalysts, the incorporation of Ru notably improved the H_2O_2 formation rate (*kf*) with increasing Ru content up to a maximum at $x = 0.012$ *wt*.% and $x = 0.019$ *wt*.% for *x*Ru-BCN and *x*Ru-TCN, respectively, while it further decreased for higher Ru contents. Thus, the 0.012Ru-BCN and 0.019Ru-TCN catalysts displayed the highest *kf* in

343 their respective series, namely 3.19 ± 0.06 and 5.61 ± 0.16 μM.min^{-1}, representing
344 increases of 1.4 and 2.4 times, respectively, compared to the pristine BCN reference.
345 However, the presence of Ru in bulk or exfoliated g-C_3N_4 also favoured H_2O_2
346 decomposition, with higher Ru content leading to higher *kd* values. This negative effect
347 strongly impacted the efficiency of bulk *x*Ru-BCN catalysts, compensating for the
348 positive influence of Ru presence and not allowing any bulk Ru-modified photocatalyst
349 to outperform the BCN reference in terms of amount of H_2O_2 produced (Fig. 4a). By
350 contrast, at ultra-low Ru content (x ≤ 0.0019 *wt*.%), the exfoliated g-C_3N_4 catalyst
351 enhanced significantly H_2O_2 synthesis efficiency more than it accelerated decomposition.
352 Indeed, for the most efficient system, the 0.0019Ru-TCN photocatalyst, *kd* and *kf*
353 increased by a factor x 1.3 and x 2.2, respectively, compared to the TCN reference,
354 leading to the highest H_2O_2 accumulation after 2 h of reaction at 363 ± 9 μmol/g.

355 A denser layer stacking, a more porous structure and a larger surface area are reported
356 to reduce the charge carrier recombination and to provide more active sites accessible for
357 the reactants [12, 16, 30]. However, while exfoliated g-C_3N_4 displays those features,
358 higher H_2O_2 yields were not obtained on TCN, probably due to a lower light absorption
359 capacity (visible and UV) and the promotion of H_2O_2 decomposition. The modest
360 increase in photocatalytic activity for the *x*Ru-BCN samples suggests that the superior
361 H_2O_2 production efficiency of *x*Ru-TCN photocatalysts arises from the combined effects
362 of exfoliation and Ru incorporation. This may be linked to the presence of low-atomicity
363 Ru species detected by HAADF-STEM only on *x*Ru-TCN. Ru, known for trapping
364 electrons easily, may serve as active sites for O_2 reduction to H_2O_2. The effect is favoured
365 by highly dispersed small Ru clusters and single atoms, lowering the electron-hole pair
366 recombination and thus enhancing the H_2O_2 synthesis yield [36, 37]. However, Ru

loadings above 0.036 *wt*.% negatively affected the overall activity of *x*Ru-TCN, which could be explained by the formation of recombination centres.

Single atom catalysts have shown to exhibit higher activity and selectivity than nanoparticles, mainly due to the high dispersion of active sites. Single atom-doped g-C_3N_4 catalysts have recently been investigated for the photocatalytic synthesis of H_2O_2 [18, 38-44]. The adsorption of O_2 on dispersed single atoms has been found to be typically of an end-on type, potentially inhibiting O-O bond dissociation, restricting four-electron O_2 reduction and promoting two-electron O_2 reduction [40, 42-44]. Ohno and co-workers observed that In^{3+} and Sn^{4+} atomically inserted into g-C_3N_4 accumulated electrons during excitation, inhibiting electron-hole pair recombination and promoting the adsorption of the electrophilic O_2 and its subsequent reduction [18]. Single Sb atoms on g-C_3N_4 enhanced both O_2 reduction (to H_2O_2) and H_2O oxidation (evolving O_2) by concentrating electrons and holes at the Sb sites and melem units, respectively [40]. Single Ti atoms doping improved the photocatalytic H_2O_2 production while an optimum in Ti content was observed, favoring charge transfer and separation, and modulating the conduction band potential [41]. Also single Ni atoms increased visible light absorption, restrained charge carrier recombination, and enhanced O_2 adsorption capacity owing to the unique electronic characteristic of Ni-N_x coordination sites [43, 44]. Fe atomic sites coordinated to N and O atoms improved O_2 adsorption and activation of g-C_3N_4, as well as charge carrier separation and transfer [42]. Chu et al. anchored Co single atoms and anthraquinone on g-C_3N_4, that serve as H_2O oxidation and O_2 reduction centers, respectively [38]. Co as single atoms promoted electron/hole pair separation through hole accumulation, enhancing H_2O_2 synthesis efficiency by 4.0-fold. However, when loaded as nanoparticles, Co acted as a charge recombination center, what resulted only in a minor

391 improvement. These findings align with the present work, explaining the improvement
392 observed with *x*Ru-TCN compared to *x*Ru-BCN catalysts.
393
394 **3.2.2. Synthesis under visible light (λ > 420 nm)**
395 Fig. 5 shows to which extent the activity of the photocatalyst under visible light (λ >
396 420 nm) contributes to its overall activity obtained using the full solar spectrum.
397 Experiments were conducted with the most efficient *x*Ru-BCN and *x*Ru-TCN
398 photocatalysts, and with both reference pristine photocatalysts. Although the activity
399 decreased compared to the values achieved under solar light, all tested catalysts produced
400 H_2O_2 under visible light irradiation. Interestingly, despite their higher visible light
401 absorption, the removal of the UV-A light fraction had a more significant impact for bulk
402 g-C_3N_4 photocatalysts than for exfoliated ones. Specifically, visible light contributed for
403 12% to both the initial H_2O_2 production rate and *kf* values obtained using full-spectrum
404 light for BCN and 0.012Ru-BCN, and 18% for TCN and 0.019Ru-TCN. Similarly, visible
405 light wavelengths accounted for 35% of the H_2O_2 decomposition rate constants for BCN
406 and 0.012Ru-BCN, and 55% for their exfoliated counterparts. These data suggest that UV
407 irradiation contributed to H_2O_2 formation rather than to its decomposition, and promoted
408 especially a higher generation of electron-hole pairs in the case of bulk g-C_3N_4 catalysts,
409 involved in both H_2O_2 formation and decomposition. Furthermore, the presence of Ru led
410 to the same improvement in H_2O_2 production efficiency, regardless of whether the
411 catalysts were photoexcited by irradiation with light containing UV wavelengths or not.
412

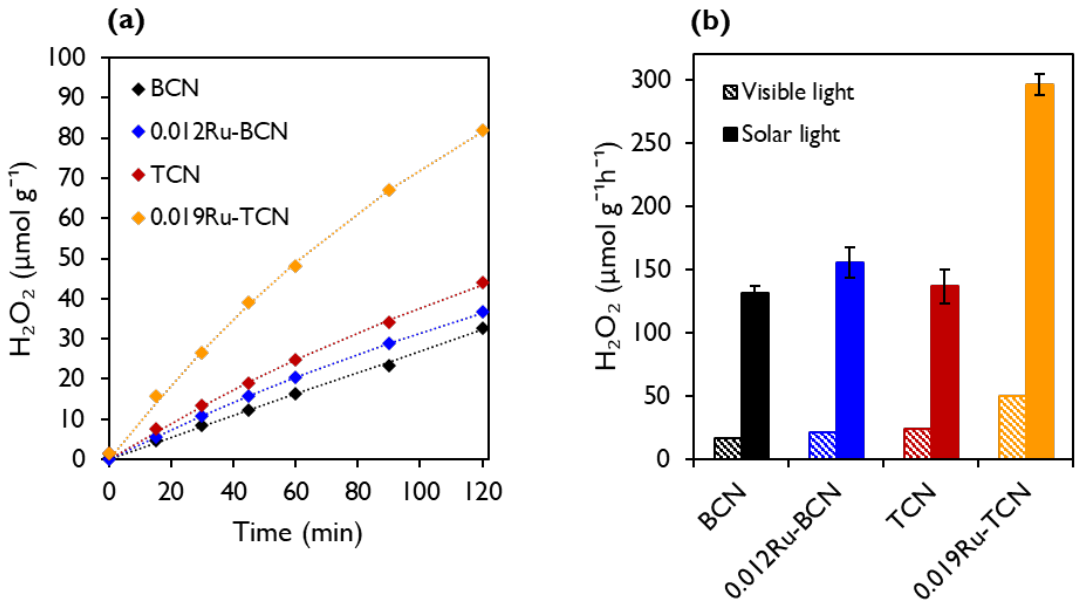

Figure 5. Photocatalytic synthesis of H_2O_2 with kinetic fitting **(a)** and initial apparent H_2O_2 production rates **(b)** over BCN (◆), 0.012Ru-BCN (◆), TCN (◆) and 0.019Ru-TCN (◆) catalysts. Experiments performed with 5% *v/v* IPA under pure visible light irradiation ($\lambda > 420$ nm). H_2O_2 production rates obtained under solar light irradiation are shown for comparison.

3.2.3. Reaction pathways

Concerning the reaction pathways, the photocatalytic synthesis of H_2O_2 is known to take place *via* reductive (reduction of O_2) and/or oxidative processes (partial oxidation of H_2O). The production of H_2O_2 through the oxidation of H_2O is a two-electron transfer process (7) competing with the oxidation of H_2O to $HO^{\bullet}$ (8), which might further react to some extent to form H_2O_2 (9), and with its complete oxidation to O_2 (10) [2].

$$2H_2O + 2h^+ \rightarrow H_2O_2 + 2H^+ \quad (7)$$

$$H_2O + h^+ \rightarrow HO^{\bullet} + H^+ \quad (8)$$

$$2HO^{\bullet} \rightarrow H_2O_2 \quad (9)$$

$$2H_2O + 4h^+ \rightarrow O_2 + 4H^+ \quad (10)$$

Regarding the generation of H_2O_2 by direct O_2 reduction, there are two main pathways, either a sequential two-step one-electron reaction (11-12), or a direct one-step two-electron process (13) [6, 34]. Although the H_2O_2 formation has not been observed on g-C_3N_4 in the absence of oxygen (*via* the water oxidation route) due to the low oxidation potential of the photogenerated holes relative to water oxidation potential, compared to other semiconductors (*e.g.*, TiO_2 or ZnO), its conduction band (−1.3 V *vs*. NHE) is suitably positioned to promote the reduction of O_2 to H_2O_2 [5, 45].

$$O_2 + e^- \rightarrow O_2^{-\bullet} \quad E° = -0.33 \text{ V } vs. \text{ NHE} \quad (11)$$

$$O_2^{-\bullet} + 2H^+ + e^- \rightarrow H_2O_2 \quad E° = +1.44 \text{ V } vs. \text{ NHE} \quad (12)$$

$$O_2 + 2e^- + 2H^+ \rightarrow H_2O_2 \quad E° = +0.68 \text{ V } vs. \text{ NHE} \quad (13)$$

To confirm the photocatalytic pathway of H_2O_2 synthesis over BCN, TCN, 0.012Ru-BCN and 0.019Ru-TCN, quenching experiments were conducted using $AgNO_3$ and *p*-BQ as electron and $O_2^{-\bullet}$ scavengers, respectively, and pure water as a control (Fig. 6). In the absence of IPA (hole scavenger), the initial H_2O_2 production rate substantially decreased to less than 25 μmol/g/h, regardless of the photocatalyst tested, indicating that photogenerated holes played an important role in the mechanism of H_2O_2 production. The holes in the valence band of g-C_3N_4 oxidize IPA to acetone (14), providing protons that are essential to form H_2O_2 [9, 12, 16]. In pure water system, protons are obtained by H_2O oxidation, for which g-C_3N_4 exhibits very low activity [46]. Moreover, IPA suppresses charge carrier recombination by scavenging photogenerated holes and increases O_2 solubility [47].

$$R–CH_2OH + 2h^+ \rightarrow R–CHO + 2H^+ \quad (14)$$

The addition of $AgNO_3$ as electron-trapping agent completely inhibited the reaction over the catalysts, demonstrating that H_2O_2 was only produced through the O_2 reduction by the photogenerated electrons and that no direct oxidation of H_2O into H_2O_2 occurred, which is in agreement with the literature [5, 45]. By contrast, with the addition of *p*-BQ, the initial H_2O_2 production rate was not completely inhibited and dropped down by 43, 54, 65 and 74% for BCN, 0.012Ru-BCN, TCN and 0.019Ru-TCN, respectively, compared to the same catalysts in pure water. This suggests that the H_2O_2 production followed partially a sequential two-step one-electron O_2 reduction route *via* the $O_2^{-\bullet}$ intermediate, as well as a one-step two-electron O_2 reduction route [6, 48]. Further, while both pathways for the reduction of O_2 into H_2O_2 occurred simultaneously on all the studied catalysts, the sequential two-step single-electron route was dominating over the one-step two-electron reaction after both thermal exfoliation and Ru incorporation into g-C_3N_4. Additionally, we cannot exclude that a small fraction of the O_2 reduced into H_2O_2 is produced by direct H_2O oxidation.

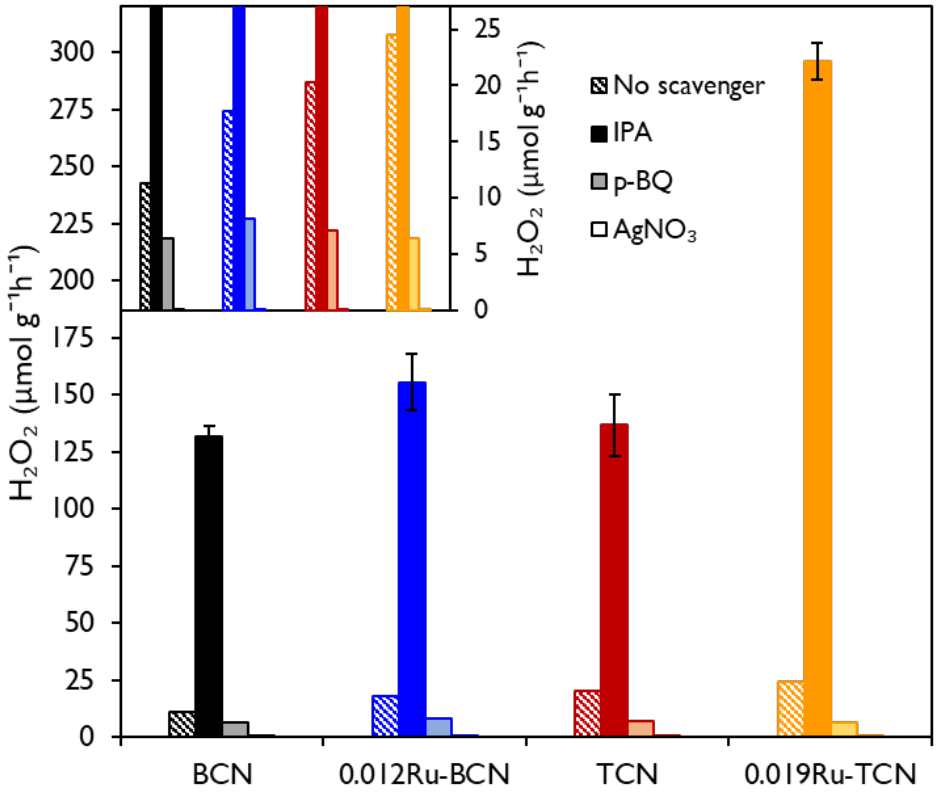

Figure 6. Initial apparent H_2O_2 production rates over BCN (◆), 0.012Ru-BCN (◆), TCN (◆) and 0.019Ru-TCN (◆) catalysts in the presence of different radical scavenger species. Inset: zoom on the low H_2O_2 production rate range (< 25 µmol/g/h). Experiments performed under simulated solar light irradiation (500 $W.m^{-2}$). Scavenger concentration: $[IPA]_0$ = 5% *v/v*, $[p\text{-}BQ]_0$ = 1 mM, $[AgNO_3]_0$ = 1 mM.

4. Conclusions

This study points out a novel method to improve the activity of g-C_3N_4 photocatalysts in the synthesis of H_2O_2 from H_2O and molecular O_2, consisting in modifying g-C_3N_4 with ultra-low amounts of Ru. Ru-modified g-C_3N_4 photocatalysts were synthesized by thermal polymerisation of the melamine precursor in the presence of ruthenium (III) acetylacetonate, followed by thermal exfoliation. Simultaneous Ru incorporation and

thermal exfoliation impacted the morphology and the structure of the g-C_3N_4 sheets, and low-atomicity Ru species were observed only in the Ru-modified exfoliated g-C_3N_4 photocatalysts. Exfoliated g-C_3N_4 with ultra-low Ru loading (0.019 *wt*.%) displayed the highest initial H_2O_2 production rate (296 ± 8 μmol/g/h) and the highest H_2O_2 formation rate constant (5.61 ± 0.16 μM/min) under simulated solar irradiation using 5% *v/v* 2-propanol as sacrificial agent and continuous air bubbling, thereby outperforming both the pristine exfoliated reference and the bulk counterpart (0.012 *wt*.% Ru). The enhanced photocatalytic efficiency was ascribed to the presence of highly dispersed small Ru nanoclusters and single atoms, reducing electron-hole pair recombination, as well as to more accessible active sites and channels for carrier migration. Quenching experiments revealed that the reaction proceeds *via* O_2 reduction following a sequential two-step single-electron route, with $O_2^{-\bullet}$ radical as an intermediate, and a one-step two-electrons pathway.

Author Contributions

The manuscript was written through the contributions of all authors. All authors have given approval to the final version of the manuscript.

CRediT author statement

Laura Valenzuela: Methodology, Investigation, Formal analysis, Funding acquisition, Writing – original draft, Supervision.

Frael-Benjamin Yimbou: Investigation.

Antoine Ewin: Investigation.

Christophe Lefèvre: Investigation.

Ramon Manzorro: Investigation.

Nicolas Keller: Conceptualization, Funding acquisition, Investigation, Formal analysis, Writing – original draft, Project administration, Supervision, Resources.

Declaration of Competing Interest

The authors declare no competing financial interest.

Data availability

Data will be made available on request.

Acknowledgements

Laura Valenzuela thanks the MOPGA program for her fellowship. R. Manzorro gratefully acknowledges financial support from Cádiz University (Young Researchers, Project PR2022-046) and National Project PID2022-142312NB-I00 funded by MCIN/AEI/10.13039/501100011033 and by "ERDF- A way of making Europe". Electron microscopy studies were performed at the DME-UCA node of the Spanish Unique Infrastructure (ICTS) on Electron Microscopy of Materials ELECMI.

References

[1] J.M. Campos-Martin, G. Blanco-Brieva, J.L.G. Fierro, Hydrogen Peroxide Synthesis: An Outlook beyond the Anthraquinone Process, Angew. Chem., Int. Ed., 45 (2006) 6962-6984. https://doi.org/10.1002/anie.200503779

[2] P. Garcia-Munoz, L. Valenzuela, D. Wegstein, T. Schanz, G.E. Lopez, A.M. Ruppert, H. Remita, J.Z. Bloh, N. Keller, Photocatalytic Synthesis of Hydrogen Peroxide from Molecular Oxygen and Water, Top. Curr. Chem., 381 (2023) 15. https://doi.org/10.1007/s41061-023-00423-y

[3] Y. Liu, Y. Zhao, J. Wang, Fenton/Fenton-like processes with in-situ production of hydrogen peroxide/hydroxyl radical for degradation of emerging contaminants: Advances and prospects, J. Hazard. Mater., 404 (2021) 124191. https://doi.org/10.1016/j.jhazmat.2020.124191

[4] T.S. Andrade, B.A.C. Sá, I.C. Sena, A.R.S. Neto, F.G.E. Nogueira, P. Lianos, M.C. Pereira, A photoassisted hydrogen peroxide fuel cell using dual photoelectrodes under tandem illumination for electricity generation, J. Electroanal. Chem., 881 (2021) 114948. https://doi.org/10.1016/j.jelechem.2020.114948

[5] R. Du, K. Xiao, B. Li, X. Han, C. Zhang, X. Wang, Y. Zuo, P. Guardia, J. Li, J. Chen, J. Arbiol, A. Cabot, Controlled oxygen doping in highly dispersed Ni-loaded g-C3N4 nanotubes for efficient photocatalytic H2O2 production, Chem. Eng. J., 441 (2022) 135999. https://doi.org/10.1016/j.cej.2022.135999

[6] S. Hu, X. Qu, P. Li, F. Wang, Q. Li, L. Song, Y. Zhao, X. Kang, Photocatalytic oxygen reduction to hydrogen peroxide over copper doped graphitic carbon nitride hollow microsphere: The effect of Cu(I)-N active sites, Chem. Eng. J., 334 (2018) 410-418. https://doi.org/10.1016/j.cej.2017.10.016

[7] Y. Wang, Y. He, Y. Chi, P. Yin, L. Wei, W. Liu, X. Wang, H. Zhang, H. Song, Construction of S-scheme p-n heterojunction between protonated g-C3N4 and α-MnS nanosphere for photocatalytic H2O2 production and in situ degradation of oxytetracycline, J. Environ. Chem. Eng., 11 (2023) 109968. https://doi.org/10.1016/j.jece.2023.109968

[8] W.-J. Ong, L.-L. Tan, Y.H. Ng, S.-T. Yong, S.-P. Chai, Graphitic Carbon Nitride (g-C3N4)-Based Photocatalysts for Artificial Photosynthesis and Environmental

561 Remediation: Are We a Step Closer To Achieving Sustainability?, Chem. Rev., 116
562 (2016) 7159-7329. https://doi.org/10.1021/acs.chemrev.6b00075

563 [9] Y. Shiraishi, S. Kanazawa, Y. Sugano, D. Tsukamoto, H. Sakamoto, S. Ichikawa, T.
564 Hirai, Highly Selective Production of Hydrogen Peroxide on Graphitic Carbon Nitride
565 (g-C3N4) Photocatalyst Activated by Visible Light, ACS Catal., 4 (2014) 774-780.
566 https://doi.org/10.1021/cs401208c

567 [10] W. Wang, C. Zhou, Y. Yang, G. Zeng, C. Zhang, Y. Zhou, J. Yang, D. Huang, H.
568 Wang, W. Xiong, X. Li, Y. Fu, Z. Wang, Q. He, M. Jia, H. Luo, Carbon nitride based
569 photocatalysts for solar photocatalytic disinfection, can we go further?, Chem. Eng. J.,
570 404 (2021) 126540. https://doi.org/10.1016/j.cej.2020.126540

571 [11] Z. Zhang, Y. Zheng, H. Xie, J. Zhao, X. Guo, W. Zhang, Q. Fu, S. Wang, Q. Xu, Y.
572 Huang, Synthesis of g-C3N4 microrods with superficial C, N dual vacancies for enhanced
573 photocatalytic organic pollutant removal and H2O2 production, J. Alloys Compd., 904
574 (2022) 164028. https://doi.org/10.1016/j.jallcom.2022.164028

575 [12] Y. Liu, Y. Zheng, W. Zhang, Z. Peng, H. Xie, Y. Wang, X. Guo, M. Zhang, R. Li,
576 Y. Huang, Template-free preparation of non-metal (B, P, S) doped g-C3N4 tubes with
577 enhanced photocatalytic H2O2 generation, J. Mater. Sci. Technol., 95 (2021) 127-135.
578 https://doi.org/10.1016/j.jmst.2021.03.025

579 [13] S. Kang, X. Liu, Z. Wang, Y. Wu, M. Dou, H. Yang, H. Zhu, D. Li, J. Dou,
580 Functionalized 2D defect g-C3N4 for artificial photosynthesis of H2O2 and
581 synchronizing tetracycline fluorescence detection and degradation, Environ. Res., 232
582 (2023) 116345. https://doi.org/10.1016/j.envres.2023.116345

583 [14] H.-i. Kim, Y. Choi, S. Hu, W. Choi, J.-H. Kim, Photocatalytic hydrogen peroxide
584 production by anthraquinone-augmented polymeric carbon nitride, Appl. Catal. B:
585 Environ., 229 (2018) 121-129. https://doi.org/10.1016/j.apcatb.2018.01.060

586 [15] H. Zhang, X. Bai, Protonated g-C3N4 coated Co9S8 heterojunction for
587 photocatalytic H2O2 production, J. Colloid Interface Sci., 627 (2022) 541-553.
588 https://doi.org/10.1016/j.jcis.2022.07.077

589 [16] S. Tong, X. Zhang, P. Yang, G-C3N4 sheet nanoarchitectonics with island-like
590 crystalline/amorphous homojunctions towards efficient H2 and H2O2 evolution,
591 Environ. Res., 236 (2023) 116805. https://doi.org/10.1016/j.envres.2023.116805

592 [17] M. Zhang, Y. Yang, X. An, J. Zhao, Y. Bao, L.-a. Hou, Exfoliation method matters:
593 The microstructure-dependent photoactivity of g-C3N4 nanosheets for water purification,
594 J. Hazard. Mater., 424 (2022) 127424. https://doi.org/10.1016/j.jhazmat.2021.127424

595 [18] Z. Teng, W. Cai, W. Sim, Q. Zhang, C. Wang, C. Su, T. Ohno, Photoexcited single
596 metal atom catalysts for heterogeneous photocatalytic H2O2 production: Pragmatic
597 guidelines for predicting charge separation, Appl. Catal. B: Environ., 282 (2021) 119589.
598 https://doi.org/10.1016/j.apcatb.2020.119589

599 [19] B. Cai, Y. Zhang, J. Feng, C. Huang, T. Ma, H. Pan, Highly efficient g-C3N4
600 supported ruthenium catalysts for the catalytic transfer hydrogenation of levulinic acid to
601 liquid fuel γ-valerolactone, Renew. Energ., 177 (2021) 652-662.
602 https://doi.org/10.1016/j.renene.2021.05.159

603 [20] K.P.J. Gustafson, A. Shatskiy, O. Verho, M.D. Kärkäs, B. Schluschass, C.-W. Tai,
604 B. Åkermark, J.-E. Bäckvall, E.V. Johnston, Water oxidation mediated by ruthenium
605 oxide nanoparticles supported on siliceous mesocellular foam, Catal. Sci. Technol., 7
606 (2017) 293-299. https://doi.org/10.1039/C6CY02121B

607 [21] M. Tahir, Triphenylphosphine ruthenium (RuP) complex anchored with exfoliated
608 g-C3N4 (ECN) with an externally reflected solar photoreactor system for highly efficient
609 solar H2 production, Chem. Eng. J., 471 (2023) 144511.
610 https://doi.org/10.1016/j.cej.2023.144511

611 [22] I. Rabani, M.S. Tahir, F. Afzal, H.B. Truong, M. Kim, Y.-S. Seo, High-efficient
612 mineralization performance of photocatalysis activity towards organic pollutants over
613 ruthenium nanoparticles stabilized by metal organic framework, J. Environ. Chem. Eng.,
614 11 (2023) 109235. https://doi.org/10.1016/j.jece.2022.109235

615 [23] Z. Wei, M. Liu, Z. Zhang, W. Yao, H. Tan, Y. Zhu, Efficient visible-light-driven
616 selective oxygen reduction to hydrogen peroxide by oxygen-enriched graphitic carbon
617 nitride polymers, Energ. Environ. Sci., 11 (2018) 2581-2589.
618 https://doi.org/10.1039/C8EE01316K

619 [24] I. Papailias, N. Todorova, T. Giannakopoulou, N. Ioannidis, N. Boukos, C.P.
620 Athanasekou, D. Dimotikali, C. Trapalis, Chemical vs thermal exfoliation of g-C3N4 for
621 NOx removal under visible light irradiation, Appl. Catal. B: Environ., 239 (2018) 16-26.
622 https://doi.org/10.1016/j.apcatb.2018.07.078

623 [25] X. Wang, K. Maeda, A. Thomas, K. Takanabe, G. Xin, J.M. Carlsson, K. Domen,
624 M. Antonietti, A metal-free polymeric photocatalyst for hydrogen production from water
625 under visible light, Nat. Mater., 8 (2009) 76-80. https://doi.org/10.1038/nmat2317

626 [26] Y.-Y. Li, B.-X. Zhou, H.-W. Zhang, S.-F. Ma, W.-Q. Huang, W. Peng, W. Hu, G.-
627 F. Huang, Doping-induced enhancement of crystallinity in polymeric carbon nitride
628 nanosheets to improve their visible-light photocatalytic activity, Nanoscale, 11 (2019)
629 6876-6885. https://doi.org/10.1039/C9NR00229D

[27] H. Sun, Y. Shi, W. Shi, F. Guo, High-crystalline/amorphous g-C3N4 S-scheme homojunction for boosted photocatalytic H2 production in water/simulated seawater: Interfacial charge transfer and mechanism insight, Appl. Surf. Sci., 593 (2022) 153281. https://doi.org/10.1016/j.apsusc.2022.153281

[28] L. Lin, W. Ren, C. Wang, A.M. Asiri, J. Zhang, X. Wang, Crystalline carbon nitride semiconductors prepared at different temperatures for photocatalytic hydrogen production, Appl. Catal. B: Environ., 231 (2018) 234-241. https://doi.org/10.1016/j.apcatb.2018.03.009

[29] A. Balakrishnan, E.S. Kunnel, R. Sasidharan, M. Chinthala, A. Kumar, 3D black g-C3N4 isotype heterojunction hydrogels as a sustainable photocatalyst for tetracycline degradation and H2O2 production, Chem. Eng. J., 475 (2023) 146163. https://doi.org/10.1016/j.cej.2023.146163

[30] G. Li, Z. Xie, S. Chai, X. Chen, X. Wang, A facile one-step fabrication of holey carbon nitride nanosheets for visible-light-driven hydrogen evolution, Appl. Catal. B: Environ., 283 (2021) 119637. https://doi.org/10.1016/j.apcatb.2020.119637

[31] X. Yuan, C. Zhou, Y. Jin, Q. Jing, Y. Yang, X. Shen, Q. Tang, Y. Mu, A.-K. Du, Facile synthesis of 3D porous thermally exfoliated g-C3N4 nanosheet with enhanced photocatalytic degradation of organic dye, J. Colloid Interface Sci., 468 (2016) 211-219. https://doi.org/10.1016/j.jcis.2016.01.048

[32] J.J. Calvino, M. López-Haro, J.M. Muñoz-Ocaña, J. Puerto, A.M. Rodríguez-Chía, Segmentation of scanning-transmission electron microscopy images using the ordered median problem, Eur. J. Oper. Res., 302 (2022) 671-687. https://doi.org/10.1016/j.ejor.2022.01.022

[33] S. Goldstein, D. Aschengrau, Y. Diamant, J. Rabani, Photolysis of Aqueous H2O2: Quantum Yield and Applications for Polychromatic UV Actinometry in Photoreactors, Environ. Sci. Technol., 41 (2007) 7486-7490. https://doi.org/10.1021/es071379t

[34] Y. Pan, X. Liu, W. Zhang, B. Shao, Z. Liu, Q. Liang, T. Wu, Q. He, J. Huang, Z. Peng, Y. Liu, C. Zhao, Bifunctional template-mediated synthesis of porous ordered g-C3N4 decorated with potassium and cyano groups for effective photocatalytic H2O2 evolution from dual-electron O2 reduction, Chem. Eng. J., 427 (2022) 132032. https://doi.org/10.1016/j.cej.2021.132032

[35] M. Teranishi, S.-i. Naya, H. Tada, In Situ Liquid Phase Synthesis of Hydrogen Peroxide from Molecular Oxygen Using Gold Nanoparticle-Loaded Titanium(IV) Dioxide Photocatalyst, J. Am. Chem. Soc., 132 (2010) 7850-7851. https://doi.org/10.1021/ja102651g

[36] L. Li, Y. Yu, S. Lin, W. Chu, D. Sun, Q. Su, S. Ma, G. Du, B. Xu, Single ruthenium atom supported on g-C3N4 as an efficient photocatalyst for nitrogen fixation in ultra-pure water, Catal. Comm., 153 (2021) 106294. https://doi.org/10.1016/j.catcom.2021.106294

[37] E.N. Ntainjua, S.J. Freakley, G.J. Hutchings, Direct Synthesis of Hydrogen Peroxide Using Ruthenium Catalysts, Top. Catal., 55 (2012) 718-722. https://doi.org/10.1007/s11244-012-9866-3

[38] C. Chu, Q. Zhu, Z. Pan, S. Gupta, D. Huang, Y. Du, S. Weon, Y. Wu, C. Muhich, E. Stavitski, K. Domen, J.-H. Kim, Spatially separating redox centers on 2D carbon nitride with cobalt single atom for photocatalytic H2O2 production, Proc. Natl. Acad. Sci., 117 (2020) 6376-6382. https://doi.org/10.1073/pnas.1913403117

[39] Q. He, J. Ding, H.-J. Tsai, Y. Liu, M. Wei, Q. Zhang, Z. Wei, Z. Chen, J. Huang, S.-F. Hung, H. Yang, Y. Zhai, Boosting photocatalytic hydrogen peroxide production by

677 regulating electronic configuration of single Sb atoms via carbon vacancies in carbon
678 nitrides, J. Colloid Interface Sci., 651 (2023) 18-26.
679 https://doi.org/10.1016/j.jcis.2023.07.168

680 [40] Z. Teng, Q. Zhang, H. Yang, K. Kato, W. Yang, Y.-R. Lu, S. Liu, C. Wang, A.
681 Yamakata, C. Su, B. Liu, T. Ohno, Atomically dispersed antimony on carbon nitride for
682 the artificial photosynthesis of hydrogen peroxide, Nat. Catal., 4 (2021) 374-384.
683 https://doi.org/10.1038/s41929-021-00605-1

684 [41] T. Wang, J. Xin, Z. Li, Y. Fan, Y. Wang, Application of single-atom Ti-doped g-
685 C3N4 in photocatalytic H2O2 production, Mater. Adv., 4 (2023) 5585-5593.
686 https://doi.org/10.1039/D3MA00606A

687 [42] M. Zhang, C. Lai, F. Xu, D. Huang, T. Hu, B. Li, D. Ma, S. Liu, Y. Fu, L. Li, L.
688 Tang, L. Chen, Ultrahigh Performance H2O2 Generation by Single-Atom Fe Catalysts
689 with N/O Bidentate Ligand via Oxalic Acid and Oxygen Molecules Activation, Small, 19
690 (2023) 2301817. https://doi.org/10.1002/smll.202301817

691 [43] X. Zhang, H. Su, P. Cui, Y. Cao, Z. Teng, Q. Zhang, Y. Wang, Y. Feng, R. Feng, J.
692 Hou, X. Zhou, P. Ma, H. Hu, K. Wang, C. Wang, L. Gan, Y. Zhao, Q. Liu, T. Zhang, K.
693 Zheng, Developing Ni single-atom sites in carbon nitride for efficient photocatalytic
694 H2O2 production, Nat. Comm., 14 (2023) 7115. https://doi.org/10.1038/s41467-023-
695 42887-y

696 [44] Y.-Z. Zhang, C. Liang, H.-P. Feng, W. Liu, Nickel single atoms anchored on
697 ultrathin carbon nitride for selective hydrogen peroxide generation with enhanced
698 photocatalytic activity, Chem. Eng. J., 446 (2022) 137379.
699 https://doi.org/10.1016/j.cej.2022.137379

[45] A. Torres-Pinto, M.J. Sampaio, C.G. Silva, J.L. Faria, A.M.T. Silva, Metal-free carbon nitride photocatalysis with in situ hydrogen peroxide generation for the degradation of aromatic compounds, Appl. Catal. B: Environ., 252 (2019) 128-137. https://doi.org/10.1016/j.apcatb.2019.03.040

[46] Y. Zhao, P. Zhang, Z. Yang, L. Li, J. Gao, S. Chen, T. Xie, C. Diao, S. Xi, B. Xiao, C. Hu, W. Choi, Mechanistic analysis of multiple processes controlling solar-driven H2O2 synthesis using engineered polymeric carbon nitride, Nat. Comm., 12 (2021) 3701. https://doi.org/10.1038/s41467-021-24048-1

[47] A. Torres-Pinto, H. Boumeriame, C.G. Silva, J.L. Faria, A.M.T. Silva, Boosting Carbon Nitride Photoactivity by Metal-Free Functionalization for Selective H2O2 Synthesis under Visible Light, ACS Sustain. Chem. Eng., 11 (2023) 894-909. https://doi.org/10.1021/acssuschemeng.2c04512

[48] H. Luo, T. Shan, J. Zhou, L. Huang, L. Chen, R. Sa, Y. Yamauchi, J. You, Y. Asakura, Z. Yuan, H. Xiao, Controlled synthesis of hollow carbon ring incorporated g-C3N4 tubes for boosting photocatalytic H2O2 production, Appl. Catal. B: Environ., 337 (2023) 122933. https://doi.org/10.1016/j.apcatb.2023.122933

Supporting Information

Ru–modified graphitic carbon nitride for the solar light–driven photocatalytic H_2O_2 synthesis

Laura Valenzuela,[a,*] Frael-Benjamin Yimbou,[a] Antoine Ewin,[a] Christophe Lefèvre,[b] Ramón Manzorro,[c] Nicolas Keller [a]

[a] Institut de Chimie et Procédés pour l'Energie, l'Environnement et la Santé (ICPEES), CNRS, Strasbourg University, 25 rue Becquerel, 67087, Strasbourg, France.

[b] Institut de Physique et de Chimie des Matériaux de Strasbourg (IPCMS), CNRS/ Strasbourg University, 23 rue du Loess, Strasbourg, France.

[c] Departamento de Ciencias de los Materiales e Ingeniería Metalúrgica y Química Inorgánica, Facultad de Ciencias, Universidad de Cádiz, Spain.

[*] *Corresponding author:* valenzuelaavila@unistra.fr (L. Valenzuela)

Contents:

SI 1 - Chemicals used

Melamine (99 *wt*.%) and hydrogen peroxide solution (30 *wt*. % in H_2O; contains inhibitor) were supplied by Sigma-Aldrich. Ruthenium (III) acetylacetonate [$Ru(acac)_3$; $Ru(C_5H_7O_2)_3$; 24 % Ru min. content] was provided by Alfa Aesar. Isopropyl alcohol (IPA; C_3H_8O; ≥99.5 *wt*.%) was acquired from VWR. Potassium hydrogen phthalate ($C_8H_5KO_4$; 99 *wt*.%), potassium iodide (KI; 99 *wt*.%), silver nitrate ($AgNO_3$; 99.9 *wt*.%) and 1,4-Benzoquinone (*p*-BQ; $C_6H_4O_2$; 99 *wt*.%) were obtained from ThermoFisher Scientific. All chemicals were used as received without any further purification. Ultrapure water (18.2 MΩ•cm) was used throughout the experiments.

SI 2 - Characterisation of Ru-modified g-C_3N_4 catalysts

The optical properties of the photocatalysts were analysed by UV-vis diffuse reflectance spectroscopy (DRS) in the wavelength range of 200-800 nm using a Perkin Elmer Lambda 950 Scan spectrophotometer equipped with an integrating sphere. The corresponding indirect band gaps were determined through Kubelka-Munk function combined with Tauc's relation and baseline method [1, 2].

N_2 adsorption-desorption isotherms were recorded on a Micromeritics ASAP 2420 analyser at -196 ℃. Prior to measurement, the samples were degassed at 150 ℃ under vacuum for 5 h. Surface areas were calculated according to the Brunauer- Emmett-Teller (BET) method using adsorption data in the 0.07-0.25 relative pressure range. The microporous contribution was estimated using the *t*-plot method. Pore size distributions were determined through the Barrett-Joyner-Halenda (BJH) method with Harkins-Jura curve between 1.7 and 300 nm diameter. Pore volumes were estimated from the volume of N_2 adsorbed at P/P_0=0.99.

SI 3 - Determination of H_2O_2 concentration

The H_2O_2 concentration was measured by iodometry. In this method, 1 mL of 0.1 M $C_8H_5KO_4$ and 1 mL of 0.4 M KI (aqueous solutions) were added to 3 mL sample, and then kept for 30 min under stirring. H_2O_2 molecules reacted with iodide anions under acidic conditions to form triiodide anions ($H_2O_2 + 3I^- + 2H^+ \rightarrow I_3^- + 2H_2O$), which display strong absorption at 350 nm. The absorbance at 350 nm was determined using a UV-1600 PC spectrophotometer (VWR). Absolute calibration of the method was achieved using standard H_2O_2 solutions.

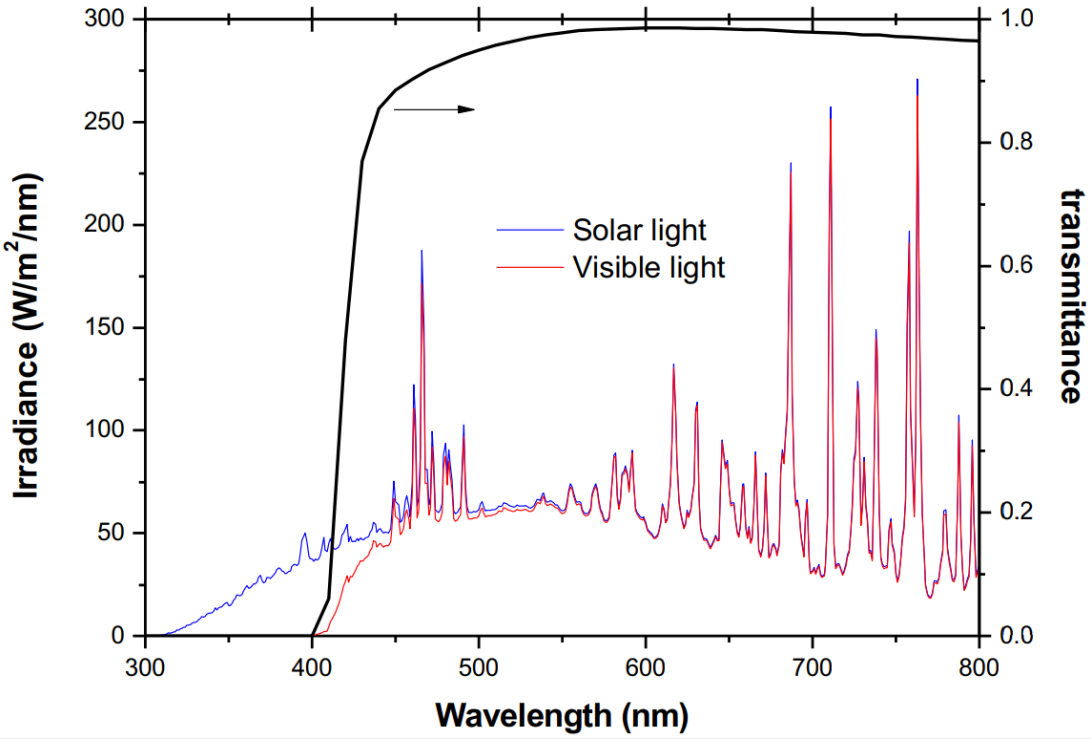

Figure S1. Emission spectra of the simulated solar (blue) and visible (red) light irradiation, and the transmittance curve of the 420 nm cut-off filter (black).

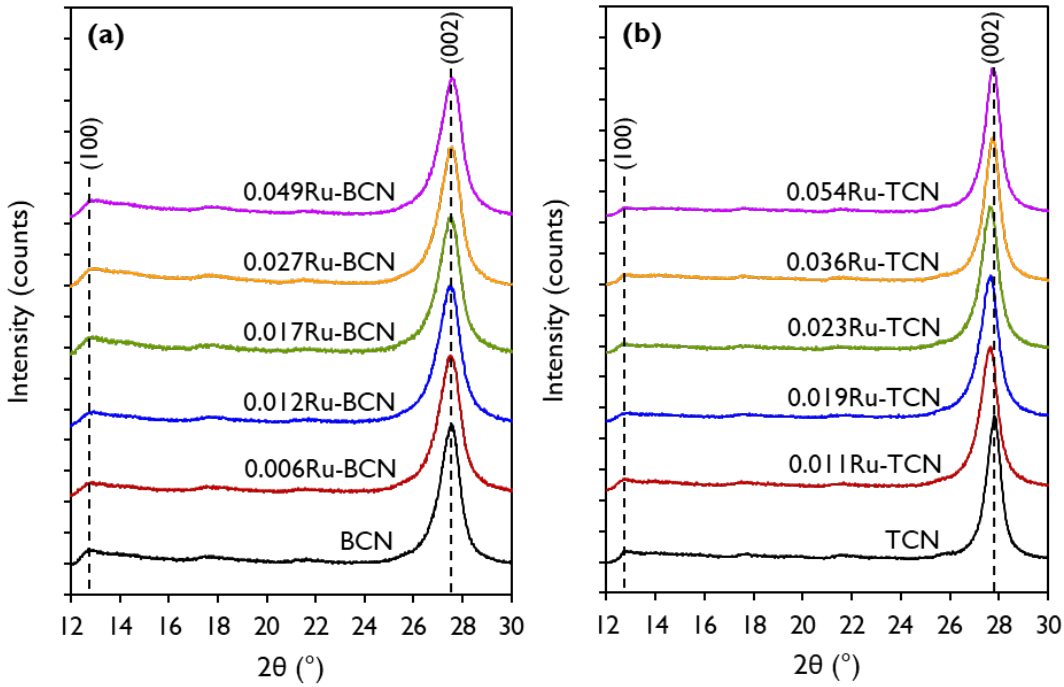

Figure S2. X-ray diffraction patterns of Ru-modified bulk g-C_3N_4, *x*Ru-BCN **(a)**, and Ru-modified exfoliated g-C_3N_4, *x*Ru-TCN **(b)**, photocatalysts.

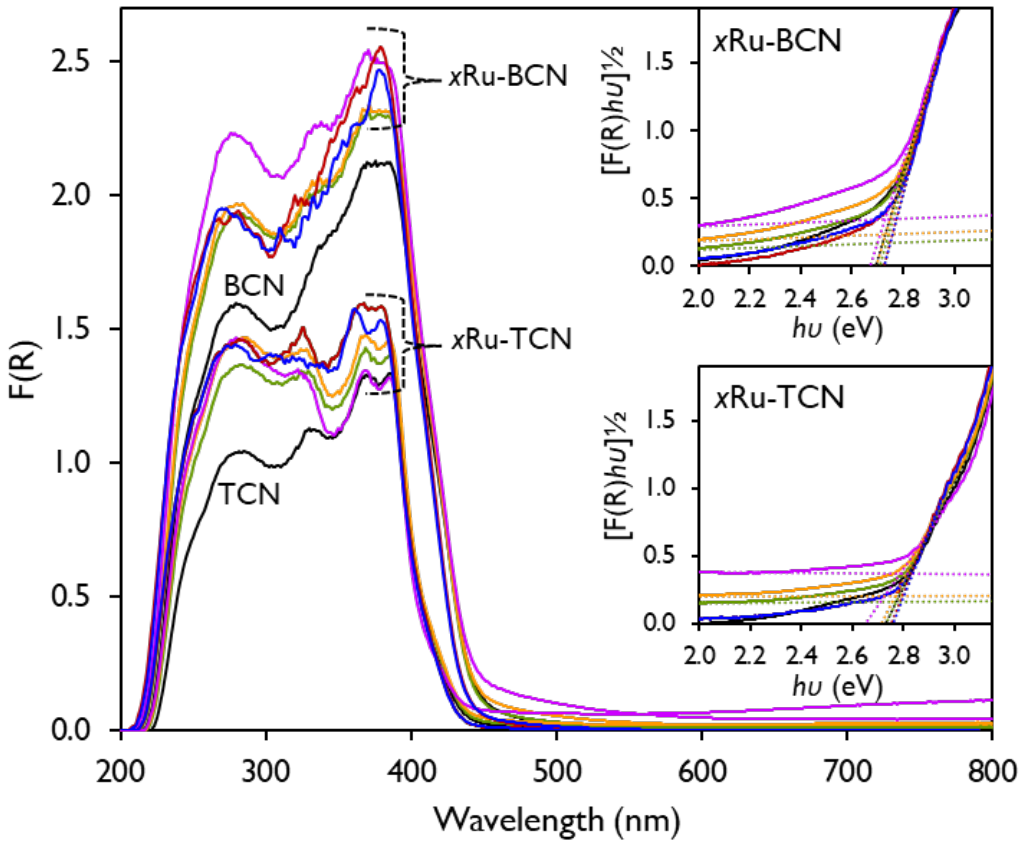

Figure S3. Kubelka-Munk curves obtained from UV-vis DRS and Tauc plots combined with the baseline method of the Kubelka-Munk function for Ru-modified bulk g-C_3N_4 (*x*Ru-BCN, *x* = 0 ◆, 0.006 ◆, 0.012 ◆, 0.017 ◆, 0.027 ◆, 0.049 ◆ *wt*.%) and Ru-modified exfoliated g-C_3N_4 (*x*Ru-TCN, *x* = 0 ◆, 0.011 ◆, 0.019 ◆, 0.023 ◆, 0.036 ◆, 0.054 ◆ *wt*.%) catalysts.

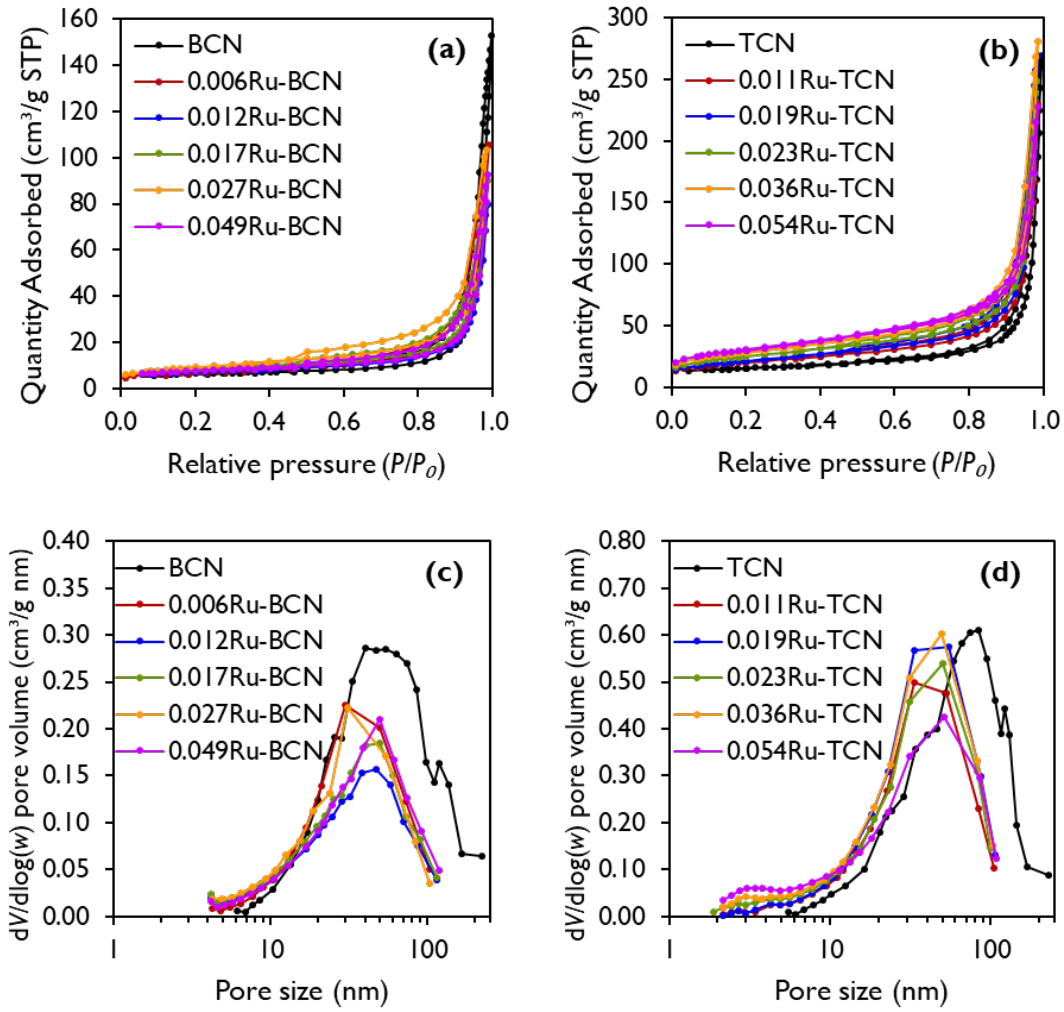

Figure S4. N_2 adsorption-desorption isotherms **(a,b)** and pore size distribution **(c,d)** of Ru-modified bulk g-C_3N_4, *x*Ru-BCN **(a,c)**, and Ru-modified exfoliated g-C_3N_4, *x*Ru-TCN **(b,d)**.

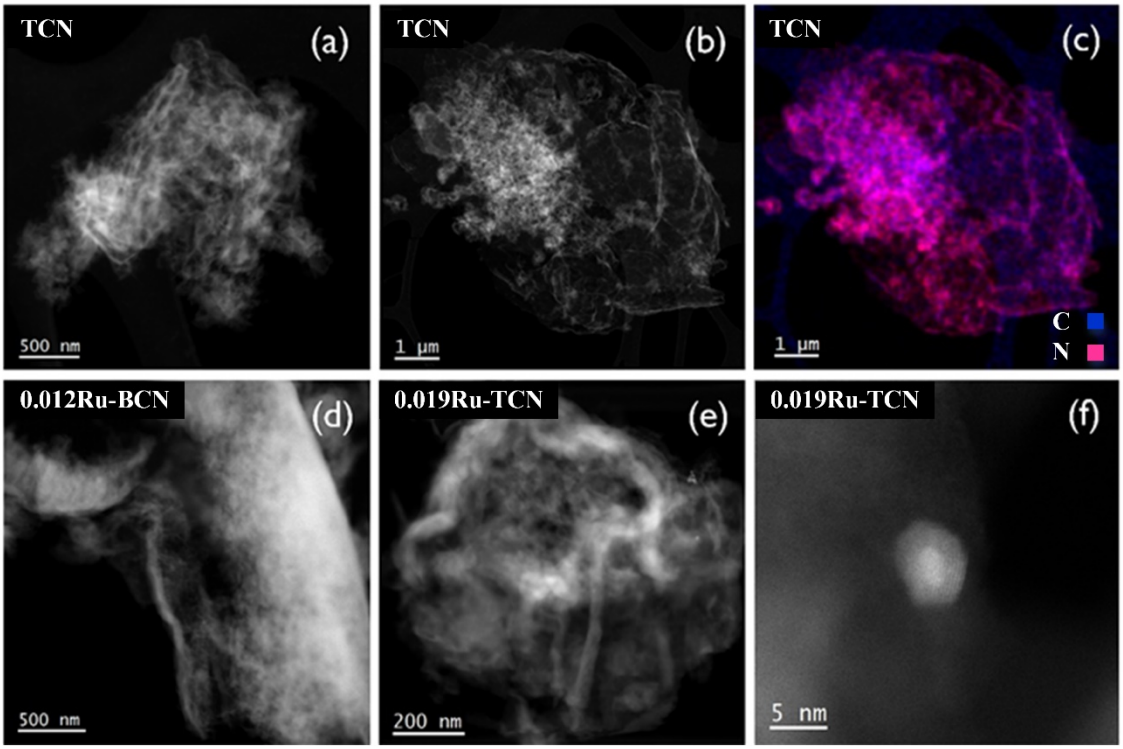

Figure S5. Low and high-magnification HAADF-STEM images, STEM–EDX elemental mapping on pristine TCN **(a-c)**, 0.012Ru-BCN **(d)** and 0.019Ru-TCN **(e,f)** photocatalysts.

References

[1] A. Escobedo-Morales, I.I. Ruiz-López, M.d. Ruiz-Peralta, L. Tepech-Carrillo, M. Sánchez-Cantú, J.E. Moreno-Orea, Automated method for the determination of the band gap energy of pure and mixed powder samples using diffuse reflectance spectroscopy, Heliyon, 5 (2019) e01505. https://doi.org/10.1016/j.heliyon.2019.e01505

[2] P. Makuła, M. Pacia, W. Macyk, How To Correctly Determine the Band Gap Energy of Modified Semiconductor Photocatalysts Based on UV–Vis Spectra, J. Phys. Chem. Lett., 9 (2018) 6814-6817. https://doi.org/10.1021/acs.jpclett.8b02892